applied sciences

MDPI

Article

A Numerical Procedure to Design a UWB Aperture-Coupled Microstrip Antenna Suitable for Space Applications

Alessandro DiCarlofelice *, Emidio DiGiampaolo and Piero Tognolatti

Department of Industrial and Information Engineering and Economics, University of L'Aquila, 67100 L'Aquila, Italy

* Correspondence: alessandro.dicarlofelice@univaq.it; Tel.: +39-0862434412

Abstract: In this paper, we show a dual-polarized ultra-wideband aperture-coupled microstrip antennae (ACMA) to be used in space missions such as CubeSat Ka-band applications. We also report the specific developed design procedure, which is distinguished from other design procedures by minimizing the complexity of construction, since it utilizes a simple multilayer structure without interlayer interconnections or inclusions. This design procedure develops an architecture for ACMA with the main objective of minimizing costs in large-scale production. The design starts from assigned specifications in terms of fractional bandwidth constrained to be larger than 40%, return loss better than 10 dB, and polarization purity and polarization isolation better than 25 dB, using materials with adequate ohmic and dielectric losses. A frequency-scaled prototype has been also designed, realized, and measured. Good agreement between the simulation and measurement results has been obtained.

Keywords: patch antenna; ultra-wideband antenna; dual polarization antenna; high polarization isolation; high polarization purity; CubeSat

check for updates

Citation: DiCarlofelice, A.; DiGiampaolo, E.; Tognolatti, P. A Numerical Procedure to Design a UWB Aperture-Coupled Microstrip Antenna Suitable for Space Applications. *Appl. Sci.* **2022**, *12*, 11243. https://doi.org/10.3390/app122111243

Academic Editors: Ernesto Limiti and Daniele Funaro

Received: 30 September 2022
Accepted: 4 November 2022
Published: 6 November 2022

Publisher's Note: MDPI stays neutral with regard to jurisdictional claims in published maps and institutional affiliations.

Copyright: © 2022 by the authors. Licensee MDPI, Basel, Switzerland. This article is an open access article distributed under the terms and conditions of the Creative Commons Attribution (CC BY) license (https://creativecommons.org/licenses/by/4.0/).

1. Introduction

After initial usage for educational and scientific purposes [1], CubeSat nanosatellite technology [2] has recently attracted interest and investments from many organizations (e.g., commercial, governmental, military) because of the low cost of launches and the availability of off-the-shelf apparatus and components. Envisaged applications span from telecommunications and remote sensing to deep-space communication and interplanetary missions [2–7]. Alongside the usual frequencies devoted to satellites links in the S-band and X-band [8–10], the Ka-band and W-band have also attracted interest for rain remote sensing (e.g., RAINCUBE) [11] and orbital debris radar [12], respectively. Different antenna concepts and developments have been discussed for CubeSat applications [13–15]. In the context of Ka-band, the development of an antenna suited for satisfying the stringent constraints of the CubeSat technology while preserving the high performance required for the specific application has been object of different investigations. A parabolic Cassegrain antenna that unfolds to be deployed has been used in [16–18] to achieve the high gain required for rain radar application. A cutting-edge reflect-array antenna printed on the back of deployable solar panels has been proposed in [19]. Phased-array technology has received attention since it ensures compactness and low weight while enabling beamforming [20,21]. A deployable active radiating array made of copper-coated polymer membranes has been developed in [22] to achieve the large aperture required for an S-band InSAR CubeSat imaging radar for earth science. An 8x8 circularly polarized array of microstrip patches with 1.5 GHz bandwidth placed on a free face of a CubeSat module was proposed in [20]. A stacked patch antenna working across the downlink and uplink Ka-bands has been proposed in [23] as an element of an array to be used in CubeSat applications.

Frequently, optimization approaches have widely been used to search for optimal solutions for specific problems. Many optimization algorithms are established based on logical strategies or numerical methods [24].

Microstrip antennae, thanks to their particular features of compactness, low profile, light weight, and moderate cost, are widely used in wireless communication systems. Their structure is suitable for dual-polarized antennae as a single patch or organized in large arrays, such as antennae for satellite synthetic aperture radars, where each element is slot-fed by means of a multilayer beamforming network. A new generation of 3D T/R modules for space applications is being developed [25–27], which requires is increasingly performance-demanding in both electrical and mechanical terms for the radiating element. The well-known aperture-coupled microstrip antennae (ACMA) first proposed by Pozar [28] have been developed into a variety of dual-polarization slot-coupled patch antennae, as reported in [29–32]. Much research has been made on dual-polarized antennae to achieve broad bandwidth, low back-radiation, low levels of cross-polarization, high efficiency, and high isolation [29–32]. Their use in polarimetric radar requires high isolation and polarization purity; many design efforts have been devoted to this theme, and a review and a comparison of cross-coupling mechanisms has been shown in [33]. The cited works show specific models of dual polarized ACMA [29–33], but they do not explicitly report the procedure followed for the design. In general, they are unable to reach wide fractional bandwidths without considerably complicating the structure, as in the case of [32], where they use via holes. We present, instead, a multi-step procedure for designing a wide fractional bandwidth ACMA with good isolation levels using simple technology that minimizes costs for large-scale production.

In this paper, we show a dual polarized high gain ACMA based on a stacked patch to be used in arrays for spaceborne applications. Since the envisaged CubeSat application has been conceived for an agile polarimetric radar at Ka-band that can arbitrarily change the working frequency and the bandwidth, we have constrained the design to match the antenna over the whole Ka-band. Therefore, we develop a specific design procedure that allows dual-polarization and ultra-wideband. It is distinguished from other design procedures by minimizing the complexity of construction, since it resorts to a simple multilayer structure without interlayer interconnections or inclusions. The developed architecture of ACMA permits minimization of the costs in large-scale production [34]. The design starts from assigned specifications in terms of fractional bandwidth constrained to be larger than 40%, return loss better than 10 dB, and polarization purity and polarization isolation better than 25 dB, using materials with adequate ohmic and dielectric losses. On the other hand, the design procedure is sufficiently general to allow simple frequency scaling so that after the design of ACMA at Ka band, which will require the use of specific technologies for realization (e.g., aerosol jet printing [35,36] or similar micro-scale digital additive manufacturing), we can use the same procedure to replicate the design at lower frequencies (i.e., 2.8–4.8 GHz). That allows us to realize the designed antenna in our laboratory and to check the obtained simulated performance by comparison with measurements. Good agreement between simulations and measurements was obtained.

2. Design Procedure

Many investigations concerning microstrip antenna and the increase of its bandwidth have been developed in the last few decades. Several solutions have been proposed, many of which are reported in [33]. Various authors have proposed the ACMA in wideband applications using different design strategies, but the basic condition for obtaining satisfactory results in increasing the bandwidth is the optimization of the set of geometrical parameters of a multilayer antenna structure. To ensure less coupling and therefore better polarization purity, we use a so-called T-shaped configuration for the slots. The basic antenna structure that we propose consists of four dielectric layers with two stacked radiating patches. The driven patch is coupled to the feed-line through a slot in a common ground plane, while the other patch is parasitic. The feeding network allows dual polarization, with two shaped slots deployed mutually orthogonal. Figure 1 shows an exploded schema of the proposed antenna together with the design parameters. For the sake of clarity, only the H-polarization parameters are shown. Those of the V-polarization will be the same, but will assume obvi-

ously different values. To distinguish them, we will use the superscript H or V above the variable name (for example, W_s^H and W_s^V). In order to achieve excellent polarization purity, the feed network is implemented in a separate layer underneath the ground plane, which has the main advantage of blocking the possible interference between the patch radiation and the parasitic radiation of the feed-lines. The increase of bandwidth in the proposed antenna is obtained using a design technique that excites three distinct resonances in the desired frequency band. The tuning of four specific geometric parameters permits the adequate collocation of the resonance frequencies to achieve the wide matching bandwidth; they are: the length of the slot, the radiating edge of the driven patch, and the size and distance from radiating edge of the parasitic patch. The thickness and the permittivity of substrate materials also play an important role in determining the bandwidth, but they may not be free to be tuned due to technological constraints.

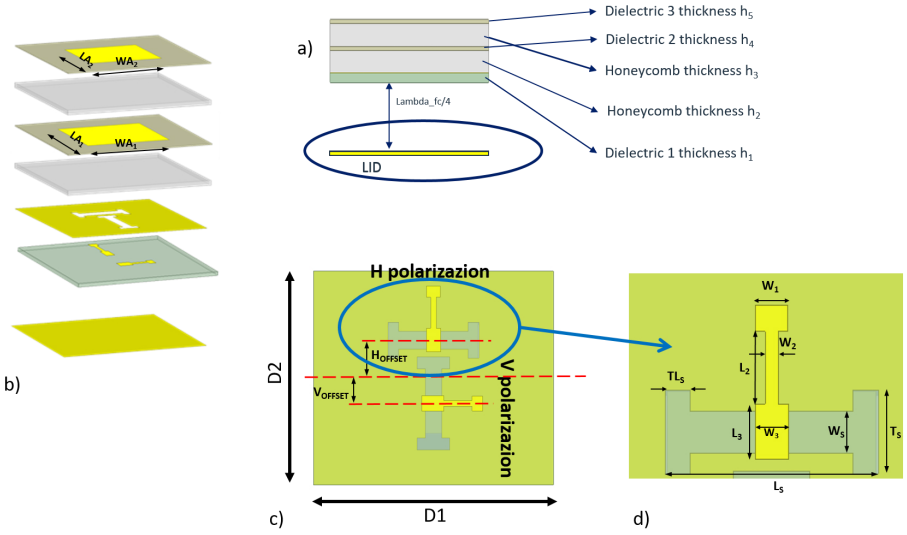


Figure 1. Geometry of the single dual-polarized patch antenna: (**a**) side view; (**b**) exploded view; (**c**) top view of the ground plane with slots and terminal part of the feeding lines; (**d**) Enlargement relative to H polarization.

The main advantage of this architecture is the simple industrial process for realizing a layered antenna structure. On the other hand, the design process requires a non-negligible effort based on an accurate cross-optimization of the slots shape, the feeding lines, and the size of patches in order to fulfill the given specifications in dual polarization condition.

In this paper, the antenna reflection coefficient for both polarizations has been optimized using the Ansys HFSS optimizer [37]. The algorithm chosen is sequential non-linear programming (SNLP) [38]. The main advantage of SNLP (gradient) is that it handles the optimization problem in more depth. This optimizer assumes that the optimization variables span a continuous space. As a result, there is no minimum step size specified in this optimizer, and the variables may take any value within the allowable constraints and within the numerical precision limits of the simulator. The optimizer modifies the variable values until the minimum is reached with acceptable accuracy.

Before starting the optimization process, the substrate (dielectric 1) must be chosen. In particular, a trade-off must be made between materials with low and high values of permittivity in order to have an antenna with high efficiency, but small size. The choice of substrate height (h_1) will also be a trade-off between line width and loss, and in some specific cases, weight. The substrates below the patches have the sole role of mechanically supporting the patches and are, therefore, chosen sufficiently thin (h_4 and h_5). Certainly, the permittivity of dielectric 2 and 3 must be chosen with sufficient stiffness to prevent patch flexing. Another important parameter to be chosen is the size of the element ($D1 \times D2$), which will have to be defined depending on if the element will be used in an array or

as a single antenna, or if beam steering is required. An important role for a wideband high-isolation ACMA antenna is fulfilled by the slots. Requiring them to be resonant without a large footprint, we have chosen them with the shape of dog-bones and with a reciprocal position between the two polarizations (V_{offset} and H_{offset}), as shown in the Figure 1c. Evidently, the X-pol of the V polarization may suffer from a slight deterioration due to the loss of symmetry of the field with respect to the axis of the patch.

The optimization procedure can be schematized as shown in the flow chart of Figure 2 and described with the following steps:

1. Choice of substrates (e.g., Rogers), heights (h_1, h_4 and h_5), and the ground-plane dimensions $D1$ and $D2$: Fix the value of the slot widths ($W_S^{H,V}$) and the size of the head ($TL_S^{H,V}$) and foot ($T_S^{H,V}$) of the dog-bone. Fix the width $W_1^{H,V}$ of the first feeding line to 50 ohms. Fix the initial lengths of the slot ($L_S^{H,V}$) and patch sizes (WA_1, WA_2, LA_1 and LA_2) all close to a quarter wavelength at center frequency;
2. Optimization of the reflection coefficient of H polarization for a 40% bandwidth: The optimized parameters are the lengths of the slot (L_S^H) and the dimension (width and length) of the second (W_2^H and L_2^H) and third feed lines (W_3^H and L_3^H) for H polarization. The size of the two patches (LA_1 and LA_2) transverse to the H-polarization slot and the two honeycomb heights (h_2 and h_3) are also optimized;
3. Once the optimization of H-polarization is finished, we deal with the optimization for V-polarization. The values obtained during the previous optimization are used for the heights (h_1 and h_2) of the two honeycomb layers. The new optimized parameters are: the V polarization length slot (L_S^V), the feed line (W_2^V, W_3^V, L_2^V and L_3^V), and patch dimensions (WA_1 and WA_2) (transverse to the V-polarization slot).

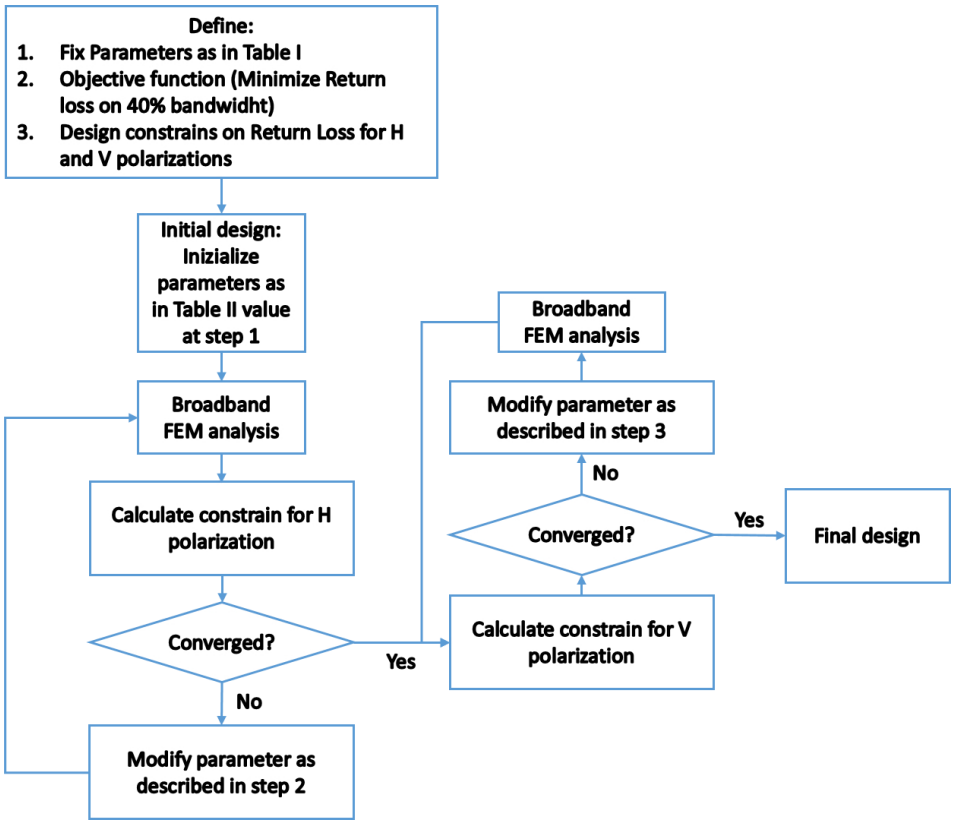


Figure 2. Flow chart of optimization procedure.

3. Analysis of Design Steps

The steps of the design procedure outlined in Section 2 are here described and discussed. First, we choose the substrates, assigning the relative dielectric constant and the loss

angle. As a possible choice, we suppose to use Rogers RT6002 ($\epsilon_r = 2.94$, $tan\delta = 0.0012$) for the dielectric 1 and the RO4003 ($\epsilon_r = 3.55$, $tan\delta = 0.0021$) for the dielectrics 2 and 3, since these materials are frequently used in space applications. The permittivity of honeycomb layers has been fixed to 1.08 and the loss angle to 8.3×10^{-4}. The fixed design parameters are reported in Table 1 and have been chosen appropriately, following the considerations discussed in the previous section. The optimized parameters are shown in Table 2 for each optimization step.

Table 1. The fixed design parameters.

Parameter	Value [mm]	Parameter	Value [mm]
h_1	0.17	T_S^H	0.96
h_4	0.02	$TL_S^{H,V}$	0.3
h_5	0.02	V_{OFFSET}	0.67
$D1$	11	H_{OFFSET}	1.01
$D2$	11	T_S^V	1.3
$W_S^{H,V}$	0.47	$W_1^{H,V}$	0.44

Table 2. The optimized parameters.

Parameter	Value at Step 1 [mm]	Value at Step 2 [mm]	Value at Step 3 [mm]
h_2	0.6	0.79	0.79
h_3	0.6	0.74	0.74
L_S^H	1.6	2.11	2.11
L_S^V	1.3	1.3	1.47
WA_1	2.59	2.59	3.2
WA_2	2.59	2.59	2.57
LA_1	2.59	3.11	3.11
LA_2	2.59	2.72	2.72
W_2^H	0.44	0.08	0.08
L_2^H	1	1.08	1.08
W_3^H	0.44	0.045	0.045
L_3^H	0.7	0.72	0.72
W_2^V	0.44	0.44	0.17
L_2^V	1.5	1.5	1.63
W_3^V	0.44	0.44	0.15
L_3^V	0.2	0.2	0.17

Figure 3 shows the results in terms of H and V return loss and H/V isolation after the first step of optimization. As one can see, the results are not good for any of the frequencies considered, although we chose the lengths of the resonant elements (patch and slot) equal to a half-wavelength at the center of the band.

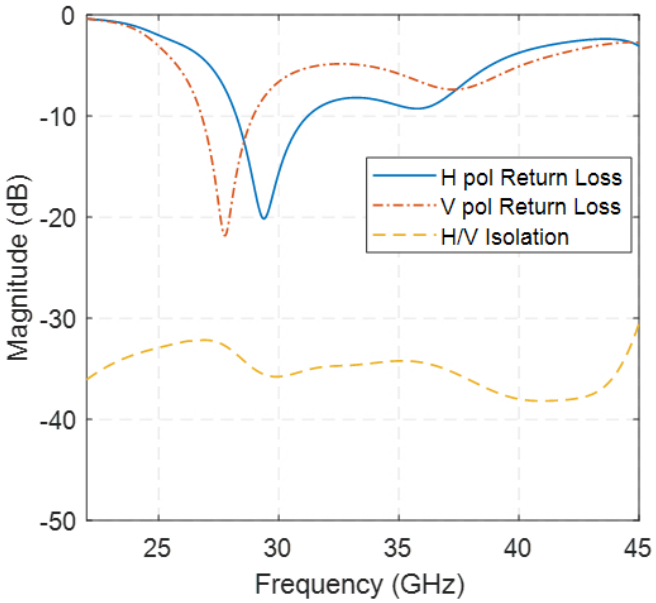


Figure 3. H and V polarization return loss and H/V isolation after first step of optimization.

Figure 4 shows the results in terms of H and V return loss and H/V isolation after the second step of optimization. H polarization has an impedance bandwidth of about 50% with a return loss of ≥10 dB.

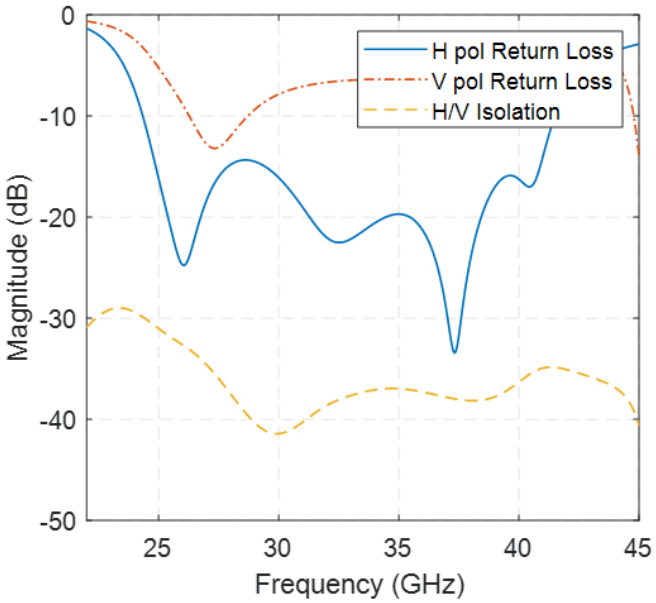


Figure 4. H and V polarization return loss and H/V isolation after second step of optimization.

Finally, Figure 5 shows the final results of optimization. The impedance has a bandwidth about 50% (2.8–4.71 GHz) for both polarizations, with a return loss ≥10 dB. The H/V isolation is greater than 30dB over the entire matching band. It can be seen in the last step of optimization that the impedance of the H polarization has remained practically unchanged. This is due to the isolation that between the two polarizations, obtained thanks to the mutual position between the two slots.

The number of iterations is variable; it depends both on the initial choice of parameters and on the width of the variability interval. On average, 150 iterations are required for the first optimization step and 100 iterations for the second step.

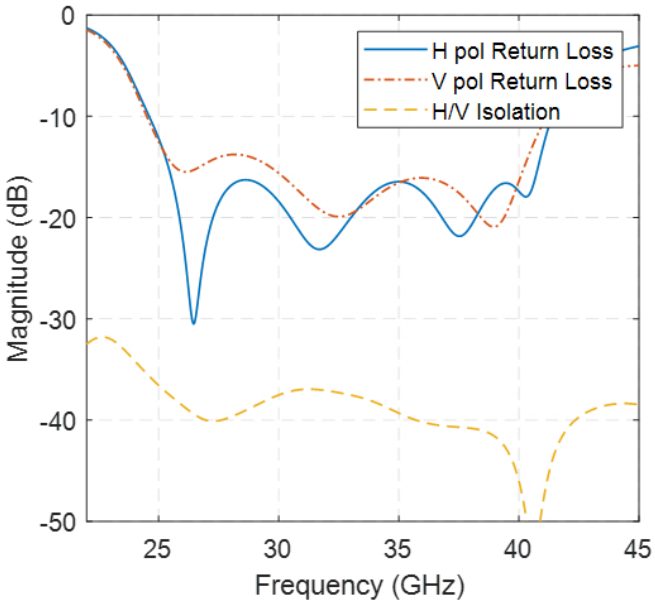


Figure 5. H and V polarization return loss and H/V isolation at the end of the optimization.

4. Design of Scaled Prototype Antenna

A prototype antenna has been designed and manufactured at 3.8 GHz center band by scaling down the model designed for Ka band. That frequency has been chosen to allow for easy and cheap realization in our laboratory. Before realization, the scaled model was numerically analyzed to determine its radiating and impedance characteristics. Similar to the previous model, we use Rogers RT6002 for the dielectric 1 and the RO4003 for the dielectrics 2 and 3, while the fixed design parameters are now scaled by the ratio between the center-band frequencies.

Evidently, the results obtained at the end of the numerical analysis are similar to those of the Ka-band. As shown in Figure 6, the matching bandwidth is about 50% (2.8–4.71 GHz) for both polarizations, with a return loss of $\geq$10 dB. The H/V isolation is greater than 30dB over the entire matching band.

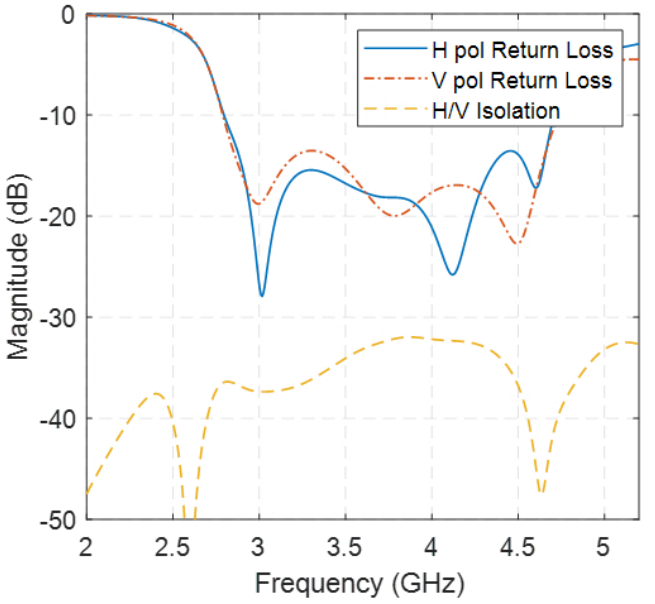


Figure 6. Scaled prototype: H and V polarization return loss and H/V isolation at the end of the optimization.

The prototype PCBs were manufactured with a CNC milling machine and are shown in Figure 7. Some polylactic acid (PLA) supports, necessary to give mechanical strength to the antenna and to allow adequate spacing between dielectrics, were fabricated with a 3D printer and are shown in the Figure 7. The lid was obtained by inserting a FR4 dielectric with a single metal face facing the feed lines.



Figure 7. Different view of realized prototype.

5. Results

The prototype antenna was measured in an anechoic chamber using the multi-probe system Starlab and other microwave facilities at MVG Italia (https://www.mvg-world.com/en (5 October 2022), as shown in Figure 8.

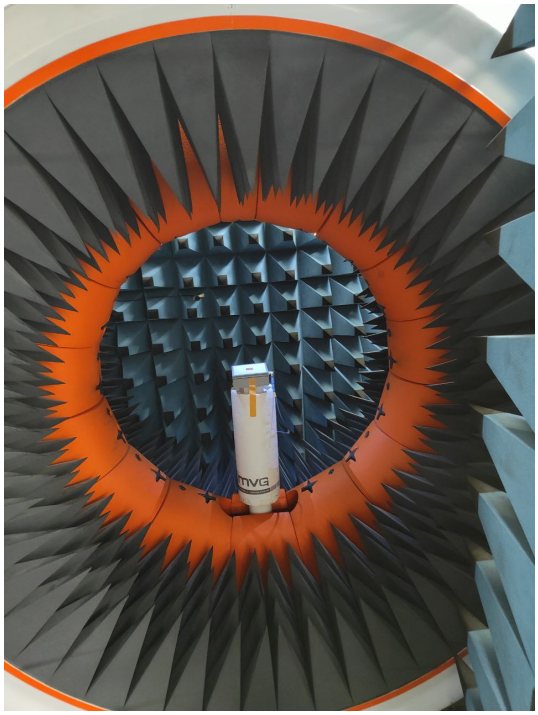


Figure 8. A picture of MVG Starlab measurement setup. The prototype antenna is over the central mast.

The simulated and experimental results (in terms of return loss and H/V isolation) of the proposed antennae are compared in Figure 9. The simulations shown in the Figure 9

also take into account the effect of the PLA supports used as a framework for the antenna. The bandwidth is almost equal to the simulation, having a slight shift upwards of 100 MHz (2.91–4.81 GHz). Meanwhile, the measured results show that the H port achieves about 49% (2.89–4.75 GHz) and the V port achieves about 48% (2.88–4.69 GHz) of the impedance bandwidth at a return loss greater than 10 dB. The measured H/V isolation is almost always greater than 30 dB, except in the initial part of the band below 3 GHz, where it reaches 25 dB.

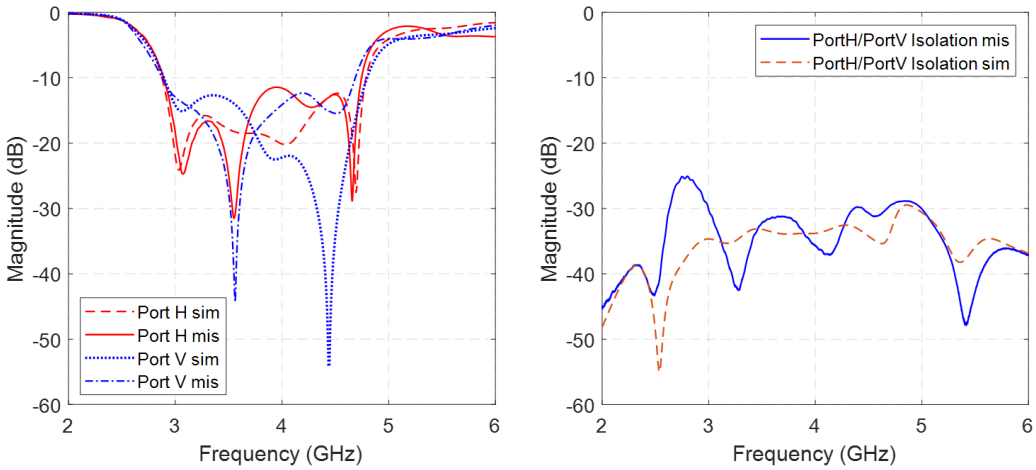


Figure 9. Scaled prototype: simulations vs. measurements. Return loss on the (**left**) and H/V isolation on the (**right**).

Additionally, the co-polar and cross-polar realized gain of the proposed antenna are measured and simulated, and results are shown in Figure 10. Simulated co-polar gain varies between 8.7 and 10.4 dBi (9.8 and 10.8 dBi), with 1.7 dB (1 dB) variation in the whole bandwidth for the H port (V port). Within the operating frequency range, measured results show that the co-polar gain of the proposed antenna is between 7 and 10.3 dBi (8.1 and 10.9 dBi), with 3.3 dB (2.8 dB) variation for the H port (V port). Simulation of cross-polar gain is always less of −30 dBi for the H Port; it is slightly higher (less than −23 dBi) for the V polarization within the operating band. The cross-polar gain difference between dual polarization is due to the position of the slot relative to the patch. In particular, while the slot of the H port is centered with respect to the $D1$ direction, the slot of the V port has an offset equal to V_{OFFSET} with respect to the D2 direction. Measured results show that the cross-polar gain of the proposed antenna is always less than −13 dBi for both polarizations. A comparison between simulated and measured realized gain and efficiency for both polarizations is shown in Figure 11. Within the operating frequency range, the measured efficiency is between 0.85–0.98 (0.78–0.997) for the H port (V port). The gain differences between the measured and simulated results come, probably, from the possible loss of symmetry of antenna geometry because of manufacturing imperfection and measurement tolerance. In addition, PLA losses, which are not perfectly known, could adversely affect the gain. Furthermore, we substituted honeycomb with air in the realized prototype. Figure 12 shows the simulated and measured results of the co-polar gain for three different frequency values—3 GHz, 3.6, and 4.5 GHz—and for H and V polarization. Good agreement between simulation and measurement results was achieved.

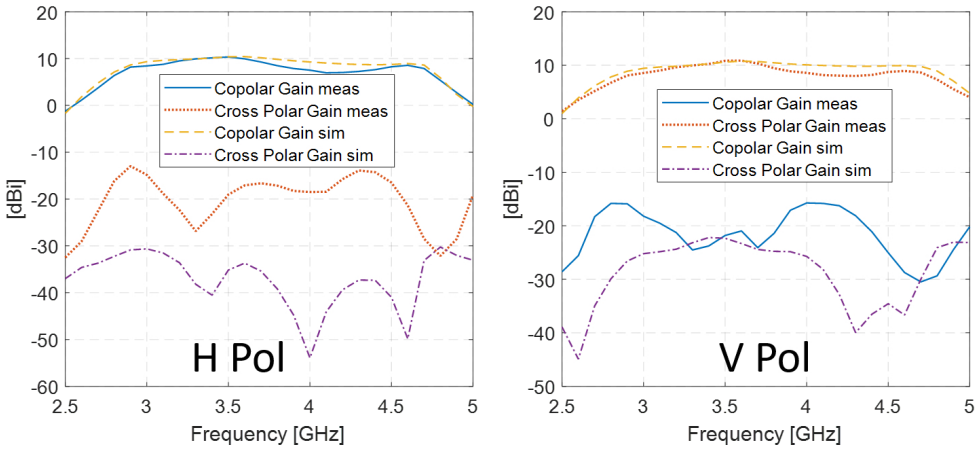


Figure 10. Scaled prototype: comparison between measurement and simulation in term of co-polar and dross-polar gain for both H/V polarizations.

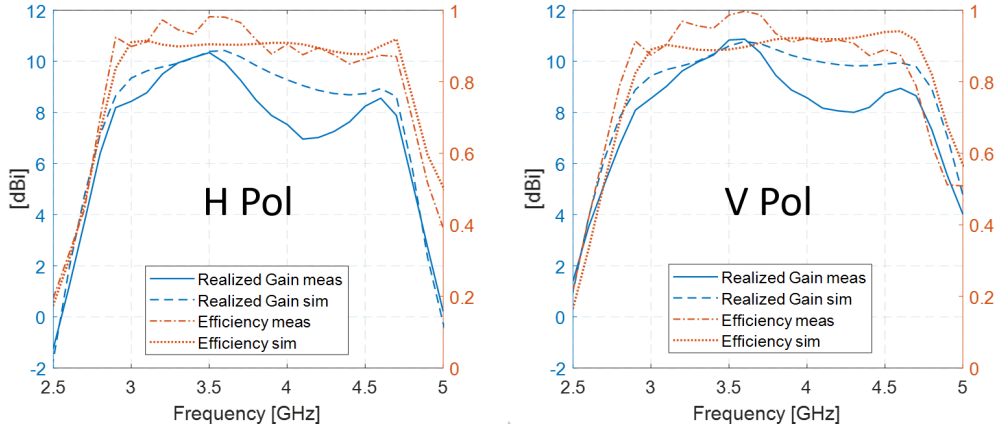


Figure 11. Scaled prototype: comparison between measurement and simulation in term of realized co-polar gain and total efficiency for both H/V polarizations.

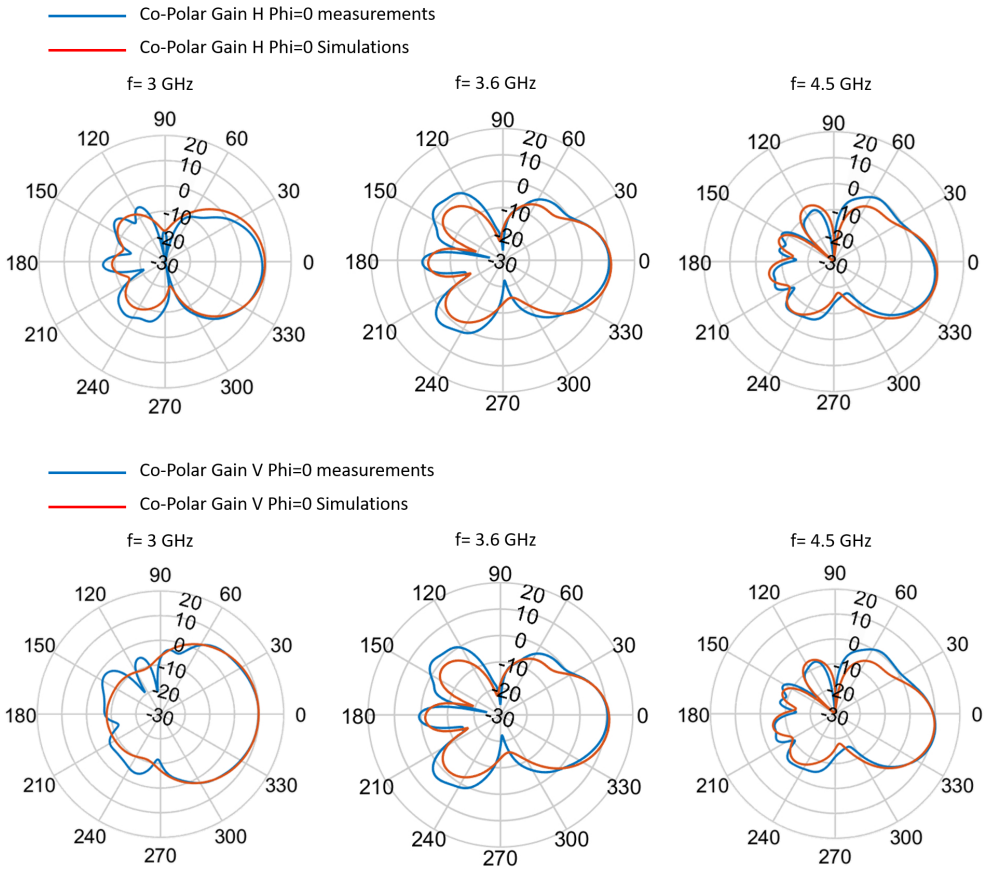


Figure 12. Scaled prototype: comparison between measurement and simulation in term of co-polar and cross-polar gain for both H/V polarizations at three different frequencies. In this case, the gain has been plotted because, in band, it is practically coincident with the realized gain.

6. Conclusions

An effective design procedure of dual-polarized ultra-wideband aperture-coupled microstrip antennae has been reported. The procedure utilizes to a constrained cross-optimization of different geometric parameters, but permits the development of a simple layered structure without inter-layer interconnects, making the antenna suitable for cost-effective mass production. Its simplicity lowers manufacturing costs while preserving robustness, and makes the antenna a candidate for space applications such as low-cost CubeSat. A scaled prototype has been designed, realized, and measured, achieving good agreement between simulation and measurement results.

Author Contributions: Conceptualization, A.D.; Formal analysis, A.D.; Methodology, A.D.; Supervision, E.D. and P.T.; Validation, E.D. and P.T.; Writing—original draft, A.D.; Writing—review & editing, E.D. All authors have read and agreed to the published version of the manuscript.

Funding: This research received no external funding.

Institutional Review Board Statement: Not applicable.

Informed Consent Statement: Not applicable.

Data Availability Statement: Not applicable.

Acknowledgments: The authors wish to thank MVG Italia for its facilities, which were used to carry out the measurements.

Conflicts of Interest: The authors declare no conflict of interest.

References

1. Viscio, M.A.; Viola, N.; Corpino, S.; Stesina, F.; Fineschi, S.; Fumenti, F.; Circi, C. Interplanetary CubeSats system for space weather evaluations and technology demonstration. *Acta Astronaut.* **2014**, *104*, 516–525. [CrossRef]
2. Capovilla, G.; Cestino, E.; Reyneri, L.M.; Romeo, G. Modular Multifunctional Composite Structure for CubeSat Applications: Preliminary Design and Structural Analysis. *Aerospace* **2020**, *7*, 17. [CrossRef]
3. Saeed, N.; Elzanaty, A.; Almorad, H.; Dahrouj, H.; Al-Naffouri, T.Y.; Alouini, M.S. CubeSat Communications: Recent Advances and Future Challenges. *IEEE Commun. Surv. Tuto.* **2020**, *22*, 1839–1862. [CrossRef]
4. Broccia, G. Cubesats in Low Earth Orbit: Perils and Countermeasures. *arXiv* **2021**, arXiv:2105.00107.
5. Cappelletti, C.; Robson, D. *CubeSat Missions and Applications*; Academic Press: Cambridge, MA, USA, 2021; pp. 53–65. [CrossRef]
6. Chahat, N.; Sauder, J.; Mitchell, M.; Beidleman, N.; Freebury, G. One-Meter Deployable Mesh Reflector for Deep-Space Network Telecommunication at *X* -Band and *Ka* -Band. *IEEE Trans. Antennas Propag.* **2020**, *68*, 727–735. [CrossRef]
7. Abulgasem, S.; Tubbal, F.; Raad, R.; Theoharis, P.I.; Lu, S.; Iranmanesh, S. Antenna Designs for CubeSats: A Review. *IEEE Access* **2021**, *9*, 45289–45324. [CrossRef]
8. Canabal, A.; Jedlicka, R.P.; Pino, A.G. Multifunctional phased array antenna design for satellite tracking. *Acta Astronaut.* **2005**, *57*, 887–900. [CrossRef]
9. Babuscia, A.; Corbin, B.; Knapp, M.; Jensen-Clem, R.; Van de Loo, M.; Seager, S. Inflatable antenna for cubesats: Motivation for development and antenna design. *Acta Astronaut.* **2013**, *91*, 322–332. [CrossRef]
10. Tubbal, F.E.; Raad, R.; Chin, K.W. A Survey and Study of Planar Antennas for Pico-Satellites. *IEEE Access* **2015**, *3*, 2590–2612. [CrossRef]
11. Peral, E.; Statham, S.; Im, E.; Tanelli, S.; Imken, T.; Price, D.; Sauder, J.; Chahat, N.; Williams, A. The Radar-in-a-Cubesat (RAINCUBE) and Measurement Results. In Proceedings of the IGARSS 2018—2018 IEEE International Geoscience and Remote Sensing Symposium, Valencia, Spain, 22–27 July 2018; pp. 6297–6300. [CrossRef]
12. Ahmed, R.; Majurec, N.; De Bleser, J.w. A CubeSat-Based Radar for Characterization of Millimetric Orbital Debris. In Proceedings of the First International Orbital Debris Conference, Sugar Land, TX, USA, 9–12 December 2019; Volume 2109, p. 6079.
13. Rahmat-Samii, Y.; Manohar, V.; Kovitz, J.M. For Satellites, Think Small, Dream Big: A review of recent antenna developments for CubeSats. *IEEE Antennas Propag. Mag.* **2017**, *59*, 22–30. [CrossRef]
14. Gao, S.; Clark, K.; Unwin, M.; Zackrisson, J.; Shiroma, W.A.; Akagi, J.M.; Maynard, K.; Garner, P.; Boccia, L.; Amendola, G.; et al. Antennas for Modern Small Satellites. *IEEE Antennas Propag. Mag.* **2009**, *51*, 40–56. [CrossRef]
15. Peral, E.; Im, E.; Wye, L.; Lee, S.; Tanelli, S.; Rahmat-Samii, Y.; Horst, S.; Hoffman, J.; Yun, S.H.; Imken, T.; et al. Radar Technologies for Earth Remote Sensing From CubeSat Platforms. *Proc. IEEE* **2018**, *106*, 404–418. [CrossRef]
16. Chahat, N.; Hodges, R.E.; Sauder, J.; Thomson, M.; Peral, E.; Rahmat-Samii, Y. CubeSat Deployable Ka-Band Mesh Reflector Antenna Development for Earth Science Missions. *IEEE Trans. Antennas Propag.* **2016**, *64*, 2083–2093. [CrossRef]
17. Chahat, N.; Hodges, R.E.; Sauder, J.; Thomson, M.; Rahmat-Samii, Y. The Deep-Space Network Telecommunication CubeSat Antenna: Using the deployable Ka-band mesh reflector antenna. *IEEE Antennas Propag. Mag.* **2017**, *59*, 31–38. [CrossRef]
18. Sauder, J.F.; Chahat, N.; Hodges, R.; Peral, E.; Rahmat-Samii, Y.; Thomson, M. Designing, Building, and Testing a Mesh Ka-band Parabolic Deployable Antenna (KaPDA) for CubeSats. In Proceedings of the 54th AIAA Aerospace Sciences Meeting, San Diego, CA, USA, 4–8 January 2016. [CrossRef]
19. Hodges, R.E.; Hoppe, D.J.; Radway, M.J.; Chahat, N.E. Novel deployable reflectarray antennas for CubeSat communications. In Proceedings of the 2015 IEEE MTT-S International Microwave Symposium, Phoenix, AZ, USA, 17–22 May 2015. [CrossRef]
20. Buttazzoni, G.; Comisso, M.; Cuttin, A.; Fragiacomo, M.; Vescovo, R.; Vincenti Gatti, R. Reconfigurable phased antenna array for extending cubesat operations to Ka-band: Design and feasibility. *Acta Astronaut.* **2017**, *137*, 114–121. [CrossRef]
21. Chahat, N. *CubeSat Antenna Design*; Wiley: New York, NY, USA, 2020. [CrossRef]
22. Wye, L.; Lee, S. *SRI CubeSat Imaging Radar for Earth Science (SRI-CIRES)*; SRI International: Menlo Park, CA, USA, 2016.
23. Simone, M.; Lodi, M.B.; Curreli, N.; Pavone, S.C.; Mazzarella, G.; Fanti, A. Optimized Design and Multiphysics Analysis of a Ka-Band Stacked Antenna for CubeSat Applications. *IEEE J. Multiscale Multiphysics Comput. Tech.* **2021**, *6*, 143–157. [CrossRef]
24. Tang, J.; Duan, D.; Xie, W. Shape Exploration and Multidisciplinary Optimization Method of Semirigid Nearing Space Airships. *J. Aircr.* **2022**, *59*, 946–963. [CrossRef]
25. Fina, A.; Marcantonio, U.D.; Suriani, A.; Mannocchi, G.; de Paulis, F.; DiCarlofelice, A.; Orlandi, A.; Tognolatti, P. An advanced transmit/receive 3D ceramic hybrid circuit module for space applications. In Proceedings of the 2015 European Microwave Conference (EuMC), Paris, France, 7–10 September 2015; pp. 785–788. [CrossRef]
26. Fina, A.; DiCarlofelice, A.; Paulis, F.D. High Power, Thermally Efficient, X-band 3D T/R Module With Calibration Capability for Space Radar. *IEEE Access* **2018**, *6*, 60921–60929. [CrossRef]
27. DiCarlofelice, A.; de Paulis, F.; Fina, A.; Marcantonio, U.D.; Orlandi, A.; Tognolatti, P. Compact and Reliable T/R Module Prototype for Advanced Space Active Electronically Steerable Antenna in 3-D LTCC Technology. *IEEE Trans. Microw. Theory Tech.* **2018**, *66*, 2746–2756. [CrossRef]
28. Pozar, D. A reciprocity method of analysis for printed slot and slot-coupled microstrip antennas. *IEEE Trans. Antennas Propag.* **1986**, *34*, 1439–1446. [CrossRef]
29. Chiou, T.W.; Wong, K.L. Broad-band dual-polarized single microstrip patch antenna with high isolation and low cross polarization. *IEEE Trans. Antennas Propag.* **2002**, *50*, 399–401. [CrossRef]

30. Sim, C.Y.D.; Chang, C.C.; Row, J.S. Dual-Feed Dual-Polarized Patch Antenna With Low Cross Polarization and High Isolation. *IEEE Trans. Antennas Propag.* **2009**, *57*, 3321–3324. [CrossRef]
31. Zaman, A.U.; Manholm, L.; Derneryd, A. Dual polarised microstrip patch antenna with high port isolation. *Electron. Lett.* **2007**, *43*, 551. [CrossRef]
32. Li, S.J.; Gao, J.; Cao, X.; Zhang, Z.; Zhang, D. Broadband and High-Isolation Dual-Polarized Microstrip Antenna With Low Radar Cross Section. *IEEE Antennas Wirel. Propag. Lett.* **2014**, *13*, 1413–1416. [CrossRef]
33. Mirmozafari, M.; Zhang, G.; Fulton, C.; Doviak, R.J. Dual-Polarization Antennas With High Isolation and Polarization Purity: A Review and Comparison of Cross-Coupling Mechanisms. *IEEE Antennas Propag. Mag.* **2019**, *61*, 50–63. [CrossRef]
34. DiCarlofelice, A.; Tognolatti, P.; Giampaolo, E.D.; Suriani, A. An Ultrawide-band Dual Polarization SAR Antenna for Space Applications. In Proceedings of the 2019 PhotonIcs & Electromagnetics Research Symposium—Spring (PIERS-Spring), Rome, Italy, 17–20 June 2019; pp. 599–603. [CrossRef]
35. He, Y.; Oakley, C.; Chahal, P.; Albrecht, J.; Papapolymerou, J. Aerosol Jet printed 24 GHz end-fire quasi-Yagi-Uda antenna on a 3-D printed cavity substrate. In Proceedings of the 2017 International Workshop on Antenna Technology: Small Antennas, Innovative Structures, and Applications (iWAT), Athens, Greece, 1–3 March 2017. [CrossRef]
36. Chletsou, A.; Crump, C.; Papapolymerou, J.; Locke, J.F. Aerosol Jet Printed Antenna for Vehicular Communications. In Proceedings of the 2020 Antenna Measurement Techniques Association Symposium (AMTA), Newport, RI, USA, 2–5 November 2020; pp. 1–4.
37. Ansys Software. Available online: https://www.ansys.com/products/electronics/ansys-hfss (accessed on 23 October 2022).
38. Powell, M.J.D. Nonlinear Programming—Sequential Unconstrained Minimization Techniques. *Comput. J.* **1969**, *12*, 207. [CrossRef]